

## **The Star Formation History of LGS 3**

B. W. Miller<sup>1</sup>, A. E. Dolphin<sup>2</sup>, M. G Lee<sup>3</sup>, S. C. Kim<sup>3</sup>, and P. Hodge<sup>4</sup>

Gemini Preprint #74

1. Gemini Observatory, AURA, Casilla 603, La Serena, Chile
2. Kitt Peak National Observatory, 950 N. Cherry Avenue, Tucson AZ 85719
3. Astronomy Program, SEES, Seoul National Observatory, Seoul 151-742, Korea
4. Astronomy Department, University of Washington, Seattle WA 98185

## The Star Formation History of LGS 3<sup>1</sup>

Bryan W. Miller

*Gemini Observatory, Casilla 603, La Serena, Chile*

Andrew E. Dolphin

*Kitt Peak National Observatory, 950 N. Cherry Ave., P.O. Box 26732, Tucson, AZ 85726, USA*

Myung Gyoon Lee, Sang Chul Kim

*Astronomy Program, SEES, Seoul National University, Seoul 151-742, Korea*

and

Paul Hodge

*Astronomy Department, University of Washington, Seattle, WA 98185, USA*

### ABSTRACT

We have determined the distance and star formation history of the Local Group dwarf galaxy LGS 3 from deep *Hubble Space Telescope* WFPC2 observations. LGS 3 is intriguing because ground-based observations showed that, while its stellar population is dominated by old, metal-poor stars, there is a handful of young, blue stars. Also, the presence of H I gas makes this a possible “transition object” between dwarf spheroidal and dwarf irregular galaxies. The *HST* data are deep enough to detect the horizontal branch and young main sequence for the first time. A new distance of  $D = 620 \pm 20$  kpc has been measured from the positions of the TRGB, the red clump, and the horizontal branch. The mean metallicity of the stars older than 8 Gyr is  $[\text{Fe}/\text{H}] = -1.5 \pm 0.3$ . The most recent generation of stars has  $[\text{Fe}/\text{H}] \approx -1$ . For the first few Gyr the global star formation rate was several times higher than the historical average and has been fairly constant since then. However, we do see significant changes in stellar populations and star formation history with radial position in the galaxy. Most of the young stars are found in the central 63 pc ( $21''$ ), where the star formation rate has been relatively constant, while the outer parts have had a declining star formation rate.

*Subject headings:* galaxies: photometry, LGS 3— galaxies: irregular — galaxies: elliptical and lenticular

## 1. Introduction

The relationship between dwarf irregular (dI) and dwarf elliptical or dwarf spheroidal (dE/dSph) galaxies is both uncertain and very important to a variety of astrophysical problems (see Ferguson & Binggeli 1994; Gallagher & Wyse 1994; Skillman & Bender 1995; Mateo 1998). Since they may be among the earliest galactic systems formed, their study is relevant to research on stellar evolution, primordial abundances and chemical evolution, and the formation of larger galaxies. Dwarf irregulars are characterized by irregular appearances, H I masses greater than about  $10^6 M_{\odot}$ , and slowly rising rotation curves. In contrast, dEs have smoother isophotes, very little H I (especially in their central regions), and undetectable rotation. If Newtonian gravity correctly describes the gravitational force law at low accelerations, then both types are dominated by dark matter. Dwarfs are the most numerous type of galaxy, and in hierarchical galaxy formation scenarios they are the building blocks of more massive galaxies.

In nearby groups and clusters of galaxies there is significant morphological segregation of dwarfs similar to that seen between giant ellipticals and spirals in dense clusters; the dEs are concentrated near the giant galaxies or the centers of the clusters while the dIs are spread throughout the volume of the group or cluster (see Ferguson & Sandage 1989; Hodge 1994). It is not known whether there was a difference in formation process or if all dwarfs formed as dIs and a fraction of them evolved into dEs. Dwarf irregulars are both bluer and of equal or lower surface brightness to the brighter dEs and so cannot evolve passively into them. Dwarf irregulars could become bright dEs if they first go through a blue compact dwarf (BCD) phase (Bothun et al. 1986). Recent evidence that BCDs are more compact than dIs of similar brightnesses (Salzer & Norton 1999) suggests that BCDs may be a special type of compact dI; their underlying stellar populations have higher central surface brightnesses and smaller scale lengths than regular dIs. Alternatively, the process that produces that starbursts in BCDs could be effective at transferring mass into the centers of the potentials. In any case, most of the gas must eventually be removed from the proto-dE either by ram-pressure stripping (Lin & Faber 1983; Kormendy 1985) and/or by winds from supernovae and massive stars (Dekel & Silk 1986; Vader 1986; Yoshii & Arimoto 1987).

However, the faded remnant of a dI may appear like the lowest surface-brightness dEs, often known as dwarfspheroidals (dSph), that tend to be close companions of large galaxies. Furthermore, the bright non-nucleated dEs in Ferguson & Sandage’s (1989) sample of Virgo and Fornax galaxies show the same spatial distribution as the dIs, suggesting that the two types may be related. These lower-mass systems would also be more easily affected by stripping and winds. A connection can also be inferred from the star formation histories of dEs in the Local Group. Galaxies like NGC 147, NGC 185, Fornax, Sextans, Leo I, Sagittarius, and Carina show star formation episodes between 2 and 6 Gyr ago (see compilations by Mateo 1998 and Grebel 1999). Thus, they were able to hold

---

<sup>1</sup>Based on observations with the NASA/ESA *Hubble Space Telescope*, obtained at the Space Telescope Science Institute, which is operated by the Association of Universities for Research in Astronomy, Inc., under NASA contract No. NAS5-26555

onto a significant amount of gas for most of their lifetimes.

Therefore, determining the evolution of different types of dwarf galaxies is significant to our understanding of the dwarfs themselves, group and cluster formation, and the morphology/density relation for dwarf galaxies. It would be especially important to study galaxies that currently have properties of both dEs and dIs. Examples of such “transition objects” in the Local Group are LGS 3, Phoenix, Antlia, DDO 210, and Pegasus (Mateo 1998). In this paper we report on the investigation of the star formation history of LGS 3 using observations from the *Hubble Space Telescope*. The high resolution and resulting photometric depth of *HST* allow the detection of stars below the horizontal branch for the first time.

Early visual inspection of photographic images of LGS 3 showed that something was unusual with its stellar population. In all previous cases, gas-rich dwarf galaxies resolved better on blue plates than visual plates, but the opposite was the case for LGS 3 (Christian & Tully 1983). The deep ground-based photometry of Lee (1995), Aparicio, Gallart, & Bertelli (1997, hereafter AGB97), and Mould (1997) show that the CMD is dominated by a red giant branch (RGB) extending up to  $I \approx 20.5$  and  $(V-I) \approx 1.3$ . Brighter and redder than this are asymptotic giant branch (AGB) stars, including carbon stars (Cook & Olszewski 1989). The color and width of the RGB led Lee (1995) to estimate that  $[\text{Fe}/\text{H}] = -2.1 \pm 0.2$ , similar to the most metal-poor Galactic globular clusters and dwarf spheroidal satellites. The relatively wide giant branch compared to globular clusters may also be indicative of a spread in age or metallicity, but photometric uncertainties made this impossible to determine. However, unlike these old systems, LGS 3 does contain several blue stars that may be young, main-sequence stars or evolved blue supergiants. A lack of detectable H II regions means that there is no current massive star formation (Hodge & Miller 1995).

Its stellar population, metallicity, and surface-brightness profile would have classified LGS 3 as a dSph. However, Thuan & Martin (1979) detected H I emission associated with LGS 3 at a heliocentric velocity of  $-280 \text{ km s}^{-1}$ ; classifying it as a dI. Lo, Sargent, & Young (1993) confirmed the H I detection with the VLA and determined that the total mass of H I is  $2 \times 10^5 M_{\odot}$  and that the dynamical mass is  $(1.8 \pm 1.0) \times 10^7 M_{\odot}$  for a distance of 760 kpc. This amount of gas is much lower than normal for a dI galaxy and the resulting mass to blue light ratio,  $26 \pm 16 M_{\odot}/L_{B,\odot}$ , is much higher than is typical for dIs. The best distance estimates put it between 770 kpc and 960 kpc using the  $I$  magnitude at the tip of the RGB (Lee 1995; AGB97; Mould 1997). Lee’s surface photometry gives  $M_V = -10.35$ , making it similar in luminosity to the Andromeda III and Sextans dSphs. Its distance and location make LGS 3 a definite member of the Local Group and it is probably a satellite of either M31 or M33 (Lee 1995).

Cook et al. (1999) have now measured the radial velocities of four giants in LGS 3. The systemic velocity of  $-282 \pm 4 \text{ km s}^{-1}$  is in very good agreement with the H I velocity and confirms that the H I is associated with the galaxy. The stellar velocity dispersion of  $7.9_{-2.9}^{+5.3} \text{ km s}^{-1}$  also agrees with the velocity dispersion of the H I, and it gives an “asymptotic”  $M/L$  (corrected for future fading)  $> 11$ , and possibly as high as 95, similar to other dSphs.

The high resolution of the *Hubble Space Telescope* now allows us to study the stellar populations of all Local Group dwarf galaxies to the depth that the Milky Way satellites could previously be studied from the ground. Detections of the horizontal branch and the main sequence give a much better picture of the star formation history of a galaxy than just the giant branch. Recent advances in stellar evolutionary models and the procedures to fit them to color-magnitude diagrams (Tolstoy & Saha 1996; Aparicio et al. 1996; Dolphin 1997; Dohm-Palmer et al. 1997; Holtzman et al. 1997; Hernandez, Valls-Gabaud, & Gilmore 1999) now allow us to make much more quantitative statements about the star formation and chemical enrichment histories of resolved galaxies. We have used the *Hubble Space Telescope* to image LGS 3 in  $V$  and  $I$  in order to see how the star formation history of this enigmatic object compares with the Local Group dwarf spheroidal and dwarf irregular galaxies. The observations are described in Section 2 and the results are presented in Section 3. The modeling procedure is described in Section 3.3 and some implications are discussed in Section 4.

## 2. Observations and Data Reduction

### 2.1. Observations and Photometry

Wide Field and Planetary Camera 2 (WFPC2) observations of LGS 3 were acquired on 1999 January 9 as part of *HST* program GO-6695. A total of 18400 seconds of integration (8 orbits) were divided evenly between the F555W and F814W filters. Two exposures were taken during each orbit to aid in the removal of cosmic rays. The requirements of avoiding bright stars that could cause either badly saturated pixels or scattered light, maximizing the scheduling windows, and imaging a large area of the galaxy resulted in the placement of the galaxy center on the WF2 detector rather than the higher-resolution PC. Figure 1 shows the WFPC2 footprint on a ground-based  $V$ -image from Lee (1995). In an effort to gain back some resolution we employed a 4 position sub-pixel dither observing scheme. The measured offsets of the dithers from the F555W PC images were  $(0''.000, 0''.000)$ ,  $(0''.498, 0''.253)$ ,  $(0''.761, 0''.754)$ , and  $(0''.255, 0''.503)$  with uncertainties of  $\pm 0.002''$ . Dithering gave the added advantage of improving the removal of cosmic rays, hot pixels, and other detector defects.

To insure the best calibration, the raw images were reprocessed using the standard pipeline tasks in STSDAS and the best available calibration files. The newly calibrated images were then reduced using three different methods and software to provide internal checks. Most of our final results come from using the HSTphot package (Dolphin 2000a).

The first step after basic calibration is to combine pairs of images taken during the same orbit in order to remove cosmic rays. Two of the reduction methods used images combined using IDL routines provided by Dr. Richard White of STScI. The third method used the HSTphot utility *crclean*. It incorporates an algorithm similar to that used in the IRAF task CRREJ; however, it is less prone to rejecting pixel from real stars in imperfectly registered images.

Photometry was done using aperture photometry on drizzled images and PSF-fitting on the un-dithered images. Drizzling combines the images taken at the four sub-pixel dither positions into an image with higher effective resolution (Gonzaga et al. 1998). The drizzling was done using standard, cookbook procedures with a pixfrac of 0.6. We were never able to produce acceptable results with PSF-fitting on the drizzled images. However, aperture photometry using methods similar to those in Miller et al. (1997) worked well in uncrowded regions. PSF-fitting is required in the crowded regions near the galaxy center. Therefore, both ALLFRAME (Stetson 1994) and HSTphot were used to do simultaneous PSF-fitting on the four dither positions.

The HSTphot package is described in detail in Dolphin (2000a), but a brief description here is warranted since it is a new package and it is the source of our final photometry. It is specifically designed to handle under-sampled WFPC2 images by using a library of TinyTim (Krist 1995) PSFs to account for variations in the PSF due to location on the chip and the centering within a pixel. After PSF-fitting corrections are also made for geometric distortion, CTE effect (Dolphin 2000b), and the 34<sup>th</sup> row effect. The four un-drizzled images in each filter were analyzed simultaneously using the *multiphot* routine to improve the signal-to-noise. A sharpness parameter and a measurement of the quality of the fit,  $\chi$ , are used for classification and to reject remaining cosmic rays and extended objects. Aperture corrections to a 0''.5 radius are calculated from all relatively isolated stars. The WF chips have many stars and the aperture correction is well determined. Unfortunately, there are not enough appropriate stars on the PC to determine accurate aperture corrections for that chip.

Artificial star tests were run in order to create a library of completeness results sampling the range of colors and magnitudes in this data. For each 0.5 mag in magnitude by 0.25 mag in color, approximately 2400 artificial stars were inserted uniformly to give a good estimate of the completeness fraction and distribution of recovered photometry. Figure 2 shows the results from the completeness tests. The 50% completeness limits are  $V_{50} \approx 27.6$  and  $I_{50} \approx 26.6$ .

## 2.2. Calibration

Each of the photometry procedures used slightly different zeropoints, but all of the calibrations used the color terms of Holtzman et al. (1995). The aperture photometry used zeropoints determined from multi-aperture photometry of bright galaxies (Whitmore et al. 1997), which are very close to the Holtzman et al. (1995) zeropoints. The ALLFRAME photometry was calibrated using the Hill et al. (1998) “long-exposure” zeropoints. The HSTphot photometry used zeropoints from Dolphin (2000b) which provides corrections to the Holtzman et al. (1995) values. We find that the three photometric methods give very good agreement in the colors, but that there are systematic offsets in the magnitudes (Table 1).

First, HSTphot magnitudes on the PC are about 0.1 magnitude brighter than those of stars in the WF chips in similar parts of the CMD. This is probably due to the larger uncertainties in the PC aperture correction. The PC contains only 11% of the total number of stars detected and

the photometry is not as deep as in the WF chips. Because of these differences and uncertainties, we do not include the PC data in the calculation of the star formation history below. Also, in the following plots that include PC data, we have added 0.1 magnitude to  $V$  and  $I$  of the PC points in order to improve the visual appearance.

For objects detected on the WF chips the agreement is excellent between HSTphot and aperture photometry. However, HSTphot gives magnitudes about 0.1 magnitude brighter in both  $V$  and  $I$  than ALLFRAME. This is probably due to differences in zeropoints and aperture corrections. The quality of the ALLFRAME and HSTphot CMDs in terms of the tightness of the RGB and the number of objects found is quite similar; both techniques do an equally good job of deblending stars. We have chosen the HSTphot results as our standard since they are based on the most recent calibration (done with the same software), the good agreement with the aperture photometry, and the ease of using HSTphot for the artificial star tests needed for the star formation history analysis. Tables of the photometry are available upon request from the author.

### 2.3. Comparison with Previous Results

In Table 1 we also compare our results with the previous ground-based work of Lee (1995), AGB97, and Mould (1997). The HSTphot results agree with Lee (1995) to within 0.02 mag. However, the HSTphot photometry is 0.07 magnitudes brighter in  $V$  and 0.02 magnitudes brighter in  $I$  than AGB97. Thus, the AGB97 results are closer to our ALLFRAME results. The Mould (1997) photometry is about 0.25 magnitudes fainter in both  $V$  and  $I$  than HSTphot. Note that in all cases the  $(V-I)$  colors agree within about 5%. This uncertainty will have no effect on the metallicity and star formation history, but it will affect the derived distance and reddening.

## 3. Results

### 3.1. The Color-Magnitude Diagram

The complete color-magnitude diagram (CMD) for LGS 3 is given in Figure 3. The main features are a narrow RGB, a few AGB stars just above the RGB, a red clump and blue loop stars, a “blue plume” of main sequence stars, and a blue horizontal branch (HB). Previous observation had identified the blue loop stars but these are the first observations to show the blue plume and horizontal branch clearly.

### 3.2. Distance and Extinction

The distance can be determined from the  $I$  magnitude at the tip of the red giant branch (TRGB), from the positions of the horizontal branch and red clump, and from matching the en-

ture CMD using the CMD modeling technique. The first three methods require an independent determination of the reddening while the CMD modeling also fits for the reddening.

The TRGB method (Lee, Freedman, & Madore 1993, hereafter LFM93; Salaris & Cassisi 1997) is an efficient and widely-used means of determining distances to resolved galaxies with old, metal-poor populations. It makes use of the fact that  $M_I$  at the helium flash (TRGB) is fairly insensitive to age and metallicity. The  $I$  magnitude of the TRGB is usually identified by a step in the luminosity function. Unfortunately, our sample of stars is too small to yield an unequivocal result; an edge-detecting Sobel filter gives a first peak at  $I = 20.1 \pm 0.2$  (Figure 4). An average of the brightest likely RGB stars gives  $I_{TRGB} = 20.12 \pm 0.26$ . There is an additional systematic error caused by Poisson statistics. If the upper RGB has  $N$  stars per magnitude, the brightest star will, on average, be  $1/N$  mags below the true tip. In this case, the TRGB is too faint by  $0.07 \pm 0.06$  mag. Thus, the TRGB is about 0.5 mag brighter than used by Lee (1995) and between 0.4 and 1.0 mag brighter than the two options considered by AGB97. The color of the TRGB is  $(V - I) = 1.50 \pm 0.05$ .

The foreground extinction towards LGS 3 has been measured to be  $A_B = 0.1$  (Burstein & Heiles 1982),  $A_B = 0.176 \pm 0.028$  (Schlegel et al. 1998), and  $A_B = 0.14 \pm 0.06$  (CMD fit, see below). Taking the mean of the latter two measurements and using  $A_B = 4.1E(B - V)$  gives a mean reddening of  $E(B - V) = 0.04 \pm 0.01$ . We assume  $R_V = 3.1$  and the reddening law of Mathis (1990) to get  $A_B = 0.16$ ,  $A_V = 0.12$  and  $A_I = 0.07$ . For comparison, Lee (1995) used  $A_V = 0.08$ , while AGB97 used  $A_V = 0.12$ . Therefore, the unreddened position of the TRGB is  $I_0 = 20.12 - 0.07 - 0.07 = 19.98 \pm 0.27$ ,  $(V - I)_0 = 1.45 \pm 0.05$ .

Continuing with the method of LFM93, the bolometric magnitude of the TRGB is determined from  $M_{bol} = -0.19[\text{Fe}/\text{H}] - 3.81$  (Da Costa & Armandroff 1990, hereafter DA90). The metallicity is calculated from relations between  $[\text{Fe}/\text{H}]$  and the  $(V - I)$  color of the RGB at  $M_I = -3.0$  (DA90) and  $M_I = -3.5$  (LFM93). We find  $(V - I)_{-3.0,0} = 1.23 \pm 0.05$  and  $(V - I)_{-3.5,0} = 1.35 \pm 0.03$ ; giving a mean metallicity of  $[\text{Fe}/\text{H}] = -1.64 \pm 0.03$  and  $M_{bol} = -3.50$ . The absolute magnitude at the TRGB is  $M_I = M_{bol} - BC_I$ , where  $BC_I = 0.881 - 0.243(V - I)_{TRGB}$  (DA90). For  $BC_I = 0.53$ , the TRGB has  $M_I = -4.03 \pm 0.15$ . The resulting distance modulus is  $(m - M)_0 = 24.08 \pm 0.30$ .

The horizontal branch is fairly flat and narrow in the  $(V, V - I)$  CMD so it can also be used as a standard candle. Twenty-one stars on the HB have  $\langle V \rangle = 24.71 \pm 0.01$  with an additional 0.05 mag of systematic error due to calibration uncertainties.  $M_V$  for the HB ranges between  $0.5 \pm 0.2$  and  $0.8 \pm 0.2$ . Dolphin et al. (2001a) find  $M_V = 0.61 \pm 0.08$  for RR Lyraes in IC 1613 whose RGB color suggests that the metallicity of its old stellar population is within 0.2 dex of that in LGS 3. Therefore, we adopt the same  $M_V$  for the horizontal branch in LGS 3. With  $A_V = 0.12$ , this gives a true distance modulus of  $(m - M)_0 = \langle V \rangle - M_V(HB) - A_V = 23.98 \pm 0.10$ .

The position of the red clump (RC) has also been used as a distance indicator (Cole 1998; Udalski 2000; Girardi & Salaris 2001). One complication is that the red clump is blended with the red end of the HB so it is difficult to disentangle the two. Fitting a quadratic plus a Gaussian

to the luminosity function in the range  $0.75 < V - I < 0.95$  and  $22 < I < 24.5$  gives  $I(RC) = 23.74 \pm 0.03$ . The semi-empirical calibration of Dolphin et al. (2001a) and Girardi & Salaris (2001) gives  $M(RC)_I = -0.29 \pm 0.10$ . Therefore, the distance modulus is  $(m - M)_0 = \langle I \rangle - M_I(RC) - A_I = 23.96 \pm 0.12$ .

Finally, the least-squares solution for the star formation history (SFH) determines the distance and reddening by fitting all parts of the CMD simultaneously. This result is not completely independent of the three previous methods since the same regions of the CMD are used. Most of the distance information will come from the positions of the HB and RC and the distance between the HB and the TRGB. Our best solution gives  $(m - M)_0 = 23.94 \pm 0.07$  and  $A_V = 0.11 \pm 0.05$ , consistent with the above estimates. Using our standard extinction of  $A_V = 0.12$  gives  $(m - M)_0 = 23.93 \pm 0.07$ . All the distance estimates are summarized in Table 2. The result from the SFH method should be roughly equivalent to averaging results from the first three methods. The weighted average of the TRGB, HB, and RC methods is  $(m - M)_0 = 23.98 \pm 0.07$ . The average of this and the result from the SFH method then gives  $(m - M)_0 = 23.96 \pm 0.07$ , corresponding to a distance of  $D = 620 \pm 20$  kpc. We adopt a larger uncertainty than given by the standard deviation since the errors are correlated. An additional source of uncertainty is the 0.1 mag of systematic error in the zeropoint calibration.

### 3.3. Procedure for Modeling the Star Formation History

A synthetic CMD-matching technique was used to study the star formation history (Dolphin 1997; Dolphin 2000c). The underlying stellar evolution models are from Girardi et al. (2000) with linear interpolation in both age and metallicity. The isochrone spacing is determined in order to adequately sample the CMD. Errors in the interpolation are between 0.01 dex and 0.05 dex in  $\log(t)$ , smaller than the age resolution used here (see Dolphin et al. 2001b). A Salpeter initial mass function is assumed. Dolphin (2000c) contains a description of the method but we have improved the determination of the chemical enrichment  $Z(t)$ . Dolphin (2000c) used multiple fits of  $\text{SFR}(t)$  for each  $((m - M)_0, A_V)$  pair, each with different  $Z(t)$  and assumed  $dZ/dt$ , to determine the best  $Z(t)$  and uncertainty. Here we make only one fit for each  $((m - M)_0, A_V)$  combination and solve for  $\text{SFR}(t, Z)$ . The step size is 0.05 mag in both distance and extinction. This allows solutions for both  $Z(t)$  and  $dZ(t)$ , the metallicity spread, which the previous method did not allow. Linear combinations of the CMDs with different ages and metallicities are then combined, while weighting by  $\text{SFR}(t)$ , to give the final synthetic CMD. The youngest age in the fits is 100 Myr since including younger ages led to a few stars in the synthetic CMD that were much brighter than any observed stars. Plotting isochrones on the observed CMD also supports this decision; there does not seem to have been any star formation in the last 100 Myr.

The observations are compared with the models in a least-squared sense using two sets of Hess diagrams ( $V - I, V, \text{Number}$ ). One is coarsely-binned (0.3 mag magnitude, 0.1 mag color) for sensitivity to large structures and one is finely-binned (0.15 mag magnitude, 0.1 mag color) for

sensitivity to smaller structures. Errors and incompleteness in the artificial CMD are derived from the artificial star tests. Rather than assigning errors from a given distribution to a discrete set of artificial stars, model CMDs are created which take into account all possible combinations of mass, age, metallicity, binarity, and photometry. Each cell in the model CMD is weighted by the completeness from the artificial star tests and then redistributed according to the distribution of the stars recovered from that cell. See Dolphin (2001) for a thorough description of the method. The models are iterated while simultaneously varying  $(m - M)_0$ ,  $A_V$ , and  $\text{SFR}(t, Z)$  to find the combination that minimizes the  $\chi^2$  difference. Because of the large uncertainties in the PC aperture corrections, we only use data from the WF chips in the modeling.

### 3.4. Star Formation History

#### 3.4.1. Global Star Formation History

The star formation rate and metallicity as a function of time for the global solution to the star formation history are given in Table 3 and shown in Figs. 5a and 6, where  $[\text{Fe}/\text{H}] = \log(Z/0.02)$ . As a whole, LGS 3 formed most of its stars very early and has had a slowly decreasing SFR for the last 10 Gyr. The procedure for determining the star formation history from matching the CMD does not make any assumptions about the chemical evolution and so does not force an increase of metallicity with time. Thus, it is possible that we can get the unphysical situation that the metallicity can decrease with time. However, the overall enrichment history is a slow and reasonable increase with time: stars older than 8 Gyr have  $[\text{Fe}/\text{H}] = -1.5 \pm 0.3$ , stars with ages between 1 and 8 Gyr have  $[\text{Fe}/\text{H}] = -1.3 \pm 0.1$ , and stars younger than 1 Gyr have  $[\text{Fe}/\text{H}] = -0.8 \pm 0.2$ , where the averages are weighted by  $(\text{SFR} \times dt)^{-1}$  and the uncertainties represent the metallicity spreads rather than real standard deviations.

Figure 7 shows the high resolution Hess diagram of the observations and the best-fit global model and an example artificial CMD from the best-fit model. The main differences between the observations and the model are: 1) the synthetic RGB is slightly too blue (although the red edge of the synthetic RGB falls in right place); 2) the synthetic RGB is too wide; 3) the RC is too sharp; 4) the HB is too weak; and 5) the MS is too blue and too strong. Some systematic effects from these mismatches are that the metallicities may be slightly off, the SFR at large ages may be underestimated, and the recent SFR may be overestimated. However, overall the match is reasonable with the maximum difference in a single grid cell being about  $3\sigma$ .

#### 3.4.2. Radial Star Formation Histories

While the global solution indicates that LGS 3 is dominated by an old stellar population, a visual inspection of the photometry suggested that there are spatial differences in the star formation

history. Therefore, we have also run SFH solutions for three radial zones and the results are shown in Table 4 and Figure 5b. In these fits,  $\text{SFR}(t)$  was solved for while keeping  $Z(t)$ ,  $dZ(t)$ ,  $(m - M)_0$ , and  $A_V$  fixed at the values from the global solution. In Figure 5b the star formation rates have been normalized to the rate in the 5–15 Gyr bin in order to show the relative rates better. The outer zone of the galaxy ( $r > 76''$ ) has had a steadily decreasing SFR and no star formation in the last 200 Myr. The intermediate zone ( $21'' < r < 76''$ ) has had a fairly constant SFR between 15 Gyr and 2 Gyr and then a decrease in the SFR by a factor of 2. The inner  $21''$  has had a fairly constant SFR throughout the lifetime of LGS 3 that is similar to or slightly higher than in the other zones. There has not been significant star formation anywhere in LGS 3 in the last 100 Myr.

Color magnitude diagrams for the three zones are shown in Figure 8. Isochrones from Girardi et al. (2000) are over-plotted after being adjusted to a distance modulus of  $(m - M)_0 = 23.96$  and a reddening of  $E(B - V) = 0.04$ . In the outer zone (Figure 8a), an extended blue HB from the oldest population is clearly visible. While most of the stars are older than 2.5 Gyr, a few stars above the HB indicate that there has been some star formation until about 500 Myr ago. The intermediate zone (Figure 8b) has the same old population but a much more pronounced blue plume from star formation within the last 2 Gyr and a few blue loop stars that are only 200–300 Myr old. Finally, the central  $21''$  of the galaxy (Figure 8c) has a higher ratio of blue to red stars than the other zones, suggesting that the bulk of the recent star formation has been in the center. The magnitudes of the brightest blue loop stars in the inner two zones suggest that the lower limit on the ages of the most recent stars is about 100 Myr. Overall, the picture of the SFH from the simple isochrone fits agrees with the detailed modeling and provides confidence that the model solution is correct. The model has the advantage of being much more quantitative.

### 3.4.3. Horizontal Branch Morphology

In order to look for a second parameter effect in the horizontal branch, we have measured two indices of horizontal branch type. The first is  $(N_B - N_R)/(N_B + N_V + N_R)$ , where  $N_B$ ,  $N_V$ ,  $N_R$  are the numbers of blue, variable and red HB stars, respectively (Lee, Demarque, & Zinn 1994, hereafter LDZ94). To avoid contamination from the blue plume, we do this analysis only on stars with projected radii greater than  $76''$ . There has not been a search for variable stars in LGS 3, so we select the variable candidates as those with  $0.35 < (V - I)_0 < 0.55$  and  $23.75 < I_0 < 24.5$ . Only one star is found in this region of the CMD. The red limit of the HB is taken to be  $(V - I)_0 = 0.8$ . With these constraints, the HB type index is  $-0.2 \pm 0.2$ . This is a lower limit since the number of variable stars is probably underestimated and there may be some contamination at the red end of the HB from intermediate-age stars. We take the metallicity of the old population to be  $[\text{Fe}/\text{H}] = -1.64$  from the TRGB analysis. This metallicity is on the Zinn & West (1984) scale, allowing us to compare HB type and metallicity with LDZ94. The comparison with Figure 7 of LDZ94 shows that LGS 3 falls on the sequence of  $[\text{Fe}/\text{H}]$  vs. HB type of Galactic globular clusters with galactocentric distances of between 8 and 40 kpc. LGS 3 most resembles NGC 6584 or

NGC 7006.

The second HB morphology index is  $i = N_B/(N_B + N_R)$  (Da Costa et al. 1996) where  $N_B$  and  $N_R$  are the same as defined above. For LGS 3, the lower limit for  $i$  is  $0.38 \pm 0.15$ . The HB of LGS 3 is bluer than the HBs of the M31 satellites And I ( $i = 0.13 \pm 0.01$ ; Da Costa et al. 1996) and And II ( $i = 0.17 \pm 0.02$ ; Da Costa et al. 2000). However, it is still redder than the HBs of globular clusters with similar metallicities. Da Costa et al. (2000) calculate that  $i = 1.0$  for NGC 6752 ( $[\text{Fe}/\text{H}] = -1.54$ ) and M13 ( $[\text{Fe}/\text{H}] = -1.65$ ) which have metallicities nearly the same as the oldest population in LGS 3. However, clusters of this metallicity that show a second parameter effect have much redder HBs: NGC 362 ( $[\text{Fe}/\text{H}] = -1.28$ ) has  $i = 0.04 \pm 0.02$ , while NGC 7006 ( $[\text{Fe}/\text{H}] = -1.59$ ) has  $i = 0.23 \pm 0.06$ . Therefore, there is evidence for a moderate second parameter effect in LGS 3. Again, we stress the caveat that HB morphologies in galaxies with more than simple stellar populations such as And I, And II, and LGS 3 are uncertain because of possible contamination of the red side of the HB from younger populations.

#### 3.4.4. Clusters of Young Stars

It is also informative to look at the spatial distributions of stars in various parts of the complete CMD. For example, Figure 9 shows the very even distribution of the oldest stars on the HB. This is the most uniform of any population. Alternatively, the main sequence stars are the most unevenly distributed (Figure 10). The young stars are concentrated towards the center of LGS 3 and are clearly grouped into clusters or associations. We have identified possible clusters using the Path Linkage Criterion (Battinelli 1991) on stars in WF2 with  $I < 26$  and  $(V - I) < 0.3$ . Thirteen groups with more than 5 stars are found with a characteristic scale of  $d_s = 4.1$  pc. The clusters are shown in Figure 11. The properties of the clusters are given in Table 5. The crosses in each region of Figure 11 are the centroids of the groups and the sigmas of the centroids in x and y. These sigmas give characteristic sizes of 2–5 pc, consistent with  $d_s$ . Table 5 also gives the distances between the most widely separated stars in each group. The largest have diameters of about 25 pc. Figure 12 shows the CMD of the stars in the largest of these clusters, Cluster 9, and a comparably sized background region. The cluster has a blue plume, a weak RGB, and a red HB. Comparison with isochrones suggests that the cluster is on the order of 800 Myr old.

## 4. Discussion

### 4.1. Distance

The new distance modulus of  $(m - M)_0 = 23.96 \pm 0.07$  (620 kpc) is considerably smaller than the previous values of  $24.5 \pm 0.2$  (810 kpc; Lee 1995),  $24.4 \pm 0.2$  (770 kpc; AGB97), and  $24.6 \pm 0.4$  (830 kpc; Mould 1997). While our TRGB distance is rather uncertain, use of the HB and the RC

should make our distance the most reliable to date. While the new distance requires adjustments to most of the physically derived parameters of LGS 3, it does not radically alter the character or location of the galaxy. The observed structural and kinematic properties and updated derived physical parameters are given in Table 6.

LGS 3 is located  $20^\circ$  from M31 and  $11^\circ$  from M33, and the three galaxies have systemic velocities with respect to the center of the Local Group of  $-59 \text{ km s}^{-1}$ ,  $-26 \text{ km s}^{-1}$ , and  $48 \text{ km s}^{-1}$ , respectively (Schmidt & Boller 1992). This suggests that LGS 3 could be a satellite of either M31 or M33 (Lee 1995). Using distances to M31 and M33 of 770 kpc and 870 kpc (Mould & Kristian 1986; LFM93), we find that LGS 3 is 280 kpc from each. The main difference compared to previous results is that LGS 3 is  $\sim 100$  kpc further away from M33. This, the larger mass of M31, and the better agreement in the velocities between LGS 3 and M31, suggest that if LGS 3 is a satellite, it is probably orbiting M31.

Of course, the consequences of LGS 3 being closer are that it is smaller and fainter. The absolute magnitude within an aperture radius of  $106''$  is now  $M_V = -9.82 \pm 0.09$ , the core radius is  $R_c = 148 \pm 9$  pc, and the most likely dynamical mass is  $M = (2.6^{+4.7}_{-1.6}) \times 10^7 M_\odot$ . The quantities described as “most likely” are related to the most likely value of the stellar velocity dispersion,  $\sigma = 7.9^{+5.3}_{-2.9} \text{ km s}^{-1}$ , from Cook et al. (1999). However, since  $M/L = \rho_0/I_0 \propto \sigma^2/I_0 R_{1/2}$ , where  $\sigma$  is the velocity dispersion and  $R_{1/2}$  is the radius where the surface brightness falls to one-half of the central value (Richstone & Tremaine 1986), the central density and mass-to-light ratio increase. The integrated  $M/L$  for the most likely value of the velocity dispersion is  $(M/L)_V = 36^{+64}_{-22}$ , while the asymptotic  $M/L$ , assuming that LGS 3 will fade by a factor of 3.9, is  $(M/L)_{V,a} = 140^{+252}_{-84}$ , compared to  $(M/L)_{V,a} = 95^{+175}_{-56}$  using a distance of 810 kpc (Cook et al. 1999). This gives LGS 3 the highest asymptotic  $M/L$  of any Local Group galaxy (see Figure 4 of Cook et al. 1999). Either the dynamics are completely dominated by dark matter, the dynamics are non-Newtonian (cf. Cook et al. 1999), or it is not virialized.

#### 4.2. Comparison of the Stellar Populations and the HI distribution

LGS 3 is also rather unique in the Local Group in that it has a very smooth H I distribution that is centered on the optical galaxy (Figure 13). Figure 14 shows the H I distribution superposed on the WFPC2 mosaic. Most other star forming dwarf irregular galaxies (e.g. SagDIG, Young & Lo 1997, hereafter YL97; IC 10, Wilcots & Miller 1998) have H I holes that may be created by stellar winds or supernovae. Leo A also has a fairly symmetric H I distribution, but, like many star forming dwarfs, it has both narrow ( $\sigma \sim 5 \text{ km s}^{-1}$ ) and broad ( $\sigma \sim 10 \text{ km s}^{-1}$ ) components (Young & Lo 1996). The narrow, cold component is associated with areas of current star formation. In LGS 3, the line profiles are fit by single Gaussians with widths between 5 and  $10 \text{ km s}^{-1}$  with a median dispersion of  $8.5 \text{ km s}^{-1}$  (YL97). Some of the dwarf spheroidals such as Phoenix and Sculptor may also have associated H I (Carignan, Demers, & Côté 1991; Carignan et al. 1998; Blitz & Robishaw 2000) but those clouds are found at large projected distances from the galaxies.

The properties of the gas in LGS 3 are consistent with a lack of star formation in the last  $\sim 100$  Myr. Gas moving at  $5 \text{ km s}^{-1}$  can travel about 500 pc, or over 3 core radii and a distance larger than the diameter of most H I holes, in 100 Myr. So, any H I holes that might have been formed during the last period of significant star formation could have been filled in. The apparent lack of a cold phase to the ISM in LGS 3 suggests that the pressures are too low to contain a large amount of high density gas for forming star (YL97). Likewise, most of the gas in LGS 3 is below the gravitational instability threshold. Assuming a thin, isothermal disk, a flat rotation curve, and a velocity dispersion of  $6 \text{ km s}^{-1}$ , the disk will be unstable if the gas density exceeds

$$\Sigma_c(M_\odot \text{ pc}^{-2}) = 0.59\alpha V(\text{km s}^{-1})/R(\text{kpc}) \quad (1)$$

where  $V$  is the rotation velocity and  $\alpha$  is a dimensionless geometrical parameter with a value of 0.7 for spiral galaxies (Kennicutt 1989). At a radius of  $76''$  (228 pc), the critical density for  $V = 5 \text{ km s}^{-1}$  is  $\Sigma_c = 9 M_\odot \text{ pc}^{-2}$ . The H I column densities at this radius are  $(5 - 10) \times 10^{19} \text{ cm}^{-2}$ , or  $\Sigma = 0.4 - 0.8 M_\odot \text{ pc}^{-2}$ , a factor of 10 below the critical density. It must be noted that the resolution of the H I data is  $35''$ , so there could be small pockets of dense gas where star formation could proceed slowly.

One must also be concerned about whether the star formation that we measure is sufficient to expel all the gas from the galaxy. Young & Lo (1997) calculate that a  $10^4 M_\odot$  burst that produces 100 supernovae would provide enough energy to blow all the gas out of the galaxy. Our star formation history solution gives only  $\sim 600 M_\odot$  of stars forming in the last period of measurable star formation between 100 and 200 Myr ago. Even if all these stars formed simultaneously, this is much less than the amount needed to drive out the gas. Also, there is no other recent burst sufficiently strong to expel the current H I mass.

Since stellar winds and supernovae have had insufficient energy input to expel gas from LGS 3, much of the enriched gas from stellar evolution has remained in the galaxy. In fact, a large fraction of the current gas may have been processed through stars. The Starburst99 models for continuous star formation and  $Z = 0.001$  give an asymptotic mass-loss rate of  $0.25 \times SFR M_\odot \text{ yr}^{-1}$  (Leitherer et al. 1999). The time averaged star formation rate for LGS 3 is  $\sim 5 \times 10^{-5} M_\odot \text{ yr}^{-1}$ . Therefore, over 15 Gyr the stars of LGS 3 have expelled about  $2 \times 10^5 M_\odot$  of gas, or a little over half of the current total gas mass (Table 6). This is also consistent with the chemical evolution calculations of AGB97 which showed that for their lower distance of 770 kpc the chemical history was best fit by a zero or low outflow model. Thus, LGS 3 is close to being the ideal closed-box system.

### 4.3. Star Formation History

The star formation history of LGS 3 is dominated by a very early burst followed by a low level of continuous star formation in the center. The SFH of the outer region is similar to the other Local Group dwarf elliptical and dwarf spheroidal galaxies such as Sculptor, And I, And III, Sextans, Tucana, Draco, Ursa Minor, Phoenix, and NGC 205 (Mateo 1998). However, the continued and/or

rejuvenated star formation in the center is more typical of some of the low-mass dwarf irregular galaxies and larger dEs like Phoenix, Fornax, WLM, Antlia, and NGC 205. This stresses the similarities that LGS 3 has always had with both dE/dSph and dI galaxies.

The Phoenix dwarf is on the lists of both dE/dSph and dI galaxies with star formation histories similar to LGS 3. Like LGS 3, Phoenix has been classified as a dSph/dI galaxy (Mateo 1998). Early ground-based CMDs showed it to be dominated by old stars with a small population of young, blue stars (Canterna & Flower 1977; Ortolani & Gratton 1988; van de Rydt, Demers, & Kunkel 1991) and there have been various reports of associated H I (Carignan et al. 1991; Young & Lo 1997; St-Germain et al. 1999). Recent deep color-magnitude diagrams of Phoenix (Holtzman et al. 2000; Held et al. 1999; Martínez-Delgado et al. 1999) combined with the results presented here, only enforce the similarities. The WFPC2 CMD of Phoenix (Holtzman et al. 2000) is strikingly similar to Figure 3. The main difference is that Phoenix has a more pronounced blue plume of young stars. Using the calibration of Da Costa & Armandroff (1990) gives metallicities for the old, giant branch stars of  $-1.9 < [\text{Fe}/\text{H}] < -1.45$ , similar to that found for LGS 3 using the same technique and calibration. The overall enrichment histories of the galaxies are similar, with most of the younger stars having  $[\text{Fe}/\text{H}] < -1$ . However, about 5% of the stars in Phoenix have  $[\text{Fe}/\text{H}] > -0.5$ , more metal-rich than any of the stars in LGS 3. Overall, however, they are more alike than different.

As might be expected from these similarities, the star formation histories of LGS 3 and Phoenix have many common features. The bulk of their stars formed more than 8 Gyr ago and, like in LGS 3, the young stars in Phoenix are concentrated in the center (Martínez-Delgado et al. 1999; Held et al. 1999). Holtzman et al. (2000) computed the star formation history for the central region of Phoenix using a method similar to that employed here. Confirming earlier work, they find that the star formation rate in the center has been fairly uniform. However, comparison with Figure 5 suggests that Phoenix has had larger variations of SFR than has LGS 3 and that Phoenix has a higher fraction of stars with ages less than 3 Gyr, thus the more prominent blue plume. However, both datasets need to be modeled using the same method before very detailed comparisons can be made.

The concentration of young stars toward the center of dwarf galaxies is quite common (see Lee 1993; Minniti & Zijlstra 1996; Mateo 1998). Currently it is not known whether there is a kinematic halo/disk structure like in the Galaxy or whether this is a pure population gradient. Martínez-Delgado et al. (1999) mention several reasons for why this could happen in Phoenix: 1) all outer stars were formed in a short initial burst; 2) star formation ceased a few Gyr ago in the outer regions; and 3) star formation has been continuous but very low in the outer parts. Our SFH solutions suggest a fourth option, a more rapidly declining star formation rate with time in the outer region compared to the center. This is similar to options 2 and 3 in that star formation in the outer region seems to have stopped recently, but not a few Gyr ago, and that star formation in the outer region over the last 2 Gyr has been fairly flat but slowly declining. This assumes that the stars were formed at radii similar to where we find them today. A large early burst of star formation occurred when the gas supply was large and extended, forming a broad sheet of metal-poor stars.

As the gas supply is used up or stripped off in the outer parts, the star formation rate drops and becomes undetectable 200-500 Myr ago. Star formation becomes concentrated towards the center. Over most of the galaxy the gas density is below the critical threshold, but random motions, stellar winds, or weak interactions (if it is indeed orbiting M31) could occasionally cause small regions of gas to exceed the critical density and collapse in the central regions.

An alternative scenario is that all the star formation has occurred in the central region where the gas density will be the highest and most likely to exceed the critical threshold. Since the velocity dispersion of LGS 3 is on the order of any possible rotational velocity, it is conceivable that simple proper motions could be responsible for older stars being found at larger radii. However, simple dynamical considerations argue against this. The time for a star moving at  $8 \text{ km s}^{-1}$  to traverse the 300 pc radius of the galaxy is  $t_{cross} = 3.7 \times 10^7$  years. Thus, stars from the most recent episode of star formation 200 Myr ago have had sufficient time to diffuse throughout the galaxy if their energies permitted it. The fact that we still see a population gradient suggests that the orbits of the young stars are confined to the central region of LGS 3.

While LGS 3 is on the order of 400 crossing times old, this is insufficient time for star-star interactions to significantly affect its structure. The relaxation time, or time when stellar encounters become important, is given by

$$t_{relax} = \frac{0.1N}{\ln N} t_{cross} \quad (2)$$

(Binney & Tremaine 1987). If LGS 3 contains  $\sim 10^6$  stars, then  $t_{relax} \approx 2.7 \times 10^{11}$  years, or much longer than a Hubble time. Also, dispersion-dominated collisions between stars and gas clouds are unlikely to be important because individual cloud cores will have low masses and because the relative velocities between stars and clouds are likely to be small. Therefore, the current locations of the stars reflect the radii where they were formed.

Overall, the star formation histories of low-luminosity dwarf irregular and dwarf spheroidal galaxies are remarkably similar: the SFH is dominated by an early burst followed by low levels of star formation in the center. The main difference between dSphs like Draco and galaxies like LGS 3 or GR8, is the amount of gas that they can retain for future star formation. This may be highly dependent on environment. LGS 3, Phoenix, and many of the dIs are found throughout the Local Group and may not be satellites of a larger spiral. However, most of the dwarf spheroidals without large amounts of associated gas are found within 250 kpc of either M31 or the Galaxy. Blitz & Robishaw (2000) argue that ram-pressure stripping from the hot halos of M31 and the Galaxy can explain the loss of gas. They also find a more extended H I cloud 10.8 kpc from LGS 3 that is offset from the detection of Young & Lo (1997) by  $50 \text{ km s}^{-1}$  and that could be due to ram-pressure stripping, but the velocity offset has the opposite sign to what stripping should produce. The H I gas associated with Phoenix may also be offset from the body of the galaxy due to ram-pressure stripping (Gallart et al. 2001).

## 5. Conclusions

We have determined a new distance, reddening, and star formation history for LGS 3 from *HST* observations. Our main results are:

1. We have resolved the horizontal branch and the young main sequence for the first time.
2. The HB type index of  $-0.2 \pm 0.2$  puts LGS 3 on the sequence of  $[\text{Fe}/\text{H}]$  vs. HB type of Galactic globular clusters with galactocentric distances between 8 and 40 kpc. The HB is bluer than those of outer halo globulars or M31 dwarf spheroidal satellites.
3. The mean metallicity has increased from  $[\text{Fe}/\text{H}] = -1.5 \pm 0.3$  for stars older than 8 Gyr to  $[\text{Fe}/\text{H}] \approx -1$  for the most recent generation.
4. The new distance measured from the TRGB, the horizontal branch, and the red clump is  $D = 620 \pm 20$  kpc.
5. We have determined the star formation history of LGS 3 by quantitatively fitting the color-magnitude diagram with evolutionary models. The global star formation history is dominated by a burst at 13 – 15 Gyr and has been fairly constant since then. However, there is clear evidence for a radial dependence on the SFH. Star formation has been constant in the central  $21''$  while in the outer regions ( $r > 76''$ ) the star formation rate has been declining with time. Dynamical arguments suggest that the current locations of the stars reflect the radii where they formed.
6. There have not been sufficient bursts of star formation to expel the gas from the galaxy. Thus, a large fraction of the current H I could have been produced by stellar mass loss.
7. The closer distance makes LGS 3 less massive but more dense so the  $M/L$  ratios are in the range  $3.9 < (M/L)_{\odot V} < 535$  with a most likely value of  $(M/L)_{\odot V} = 36_{-22}^{+64}$ .

Whether classified as irregular or spheroidal, galaxies like LGS 3 are important for studying the evolution of dwarf galaxies because they are the lowest-mass galaxies that have managed to retain some H I and have star formation until very recently. Also, they appear to be nearly ideal closed-box systems. Further work to help clarify how star formation proceeds in LGS 3 would include higher resolution H I mapping, deep, wide-field imaging to determine the full extent of LGS 3 and whether it has extra-tidal stars, and more radial velocity measurements to look for changes in velocity dispersion with radius.

We would like to thank Lisa Young for providing us with H I maps of LGS 3, Paulo Battinelli for use of the PLC code, and the referee for useful suggestions. This research has made use of NASA’s Astrophysics Data System Abstract Service and Extragalactic Database (NED). BWM would like

to thank the Carnegie Institution of Washington, the Space Telescope Science Institute, and the University of Leiden for support during this project. This research was supported by the Gemini Observatory, which is operated by the Association of Universities for Research in Astronomy, Inc., under a cooperative agreement with the NSF on behalf of the Gemini partnership: the National Science Foundation (United States), the Particle Physics and Astronomy Research Council (United Kingdom), the National Research Council (Canada), CONICYT (Chile), the Australian Research Council (Australia), CNPq (Brazil) and CONICET (Argentina). MGL is supported in part by the MOST/KISTEP International Collaboration research grant (99-01-009). Finally, we are grateful for support from NASA through grants GO-6695, GO-7496, and GO-2227.06-A from the Space Telescope Science Institute, which is operated by AURA, Inc., under NASA contract NAS5-26555.

## REFERENCES

- Aparicio, A., Gallart, C., Choisi, C., & Bertelli, G. 1996, *ApJ*, 469, L97
- Aparicio, A., Gallart, C., & Bertelli, G. 1997, *AJ*, 114, 680 (AGB97)
- Battinelli, P. 1991, *A&A*, 244, 69
- Binney, J., & Tremaine, S. 1987, *Galactic Dynamics* (Princeton: Princeton), 489
- Blitz, L., & Robishaw, T. 2000, *ApJ*, 541, 675
- Bothun, G. D., Mould, J. R., Caldwell, N., & MacGillivray, H. T. 1986, *AJ*, 92, 1007
- Burstein, D., & Heiles, C. 1982, *AJ*, 87, 1165
- Canterna, R., & Flower, P. J. 1977, *ApJ*, 212, L57
- Carignan, C., Demers, S., & Côté, S. 1991, *ApJ*, 381, 13
- Carignan, C., Beaulieu, S., Côté, S., Demers, S., & Mateo, M. 1998, *AJ*, 116, 1690
- Christian, C. A., & Tully, R. B. 1983, *AJ*, 88, 934
- Cole, A. A. 1998, *ApJ*, 500, L137
- Cook, K. H., & Olszewski, E. W. 1989, *BAAS*, 21, 775
- Cook, K. H., Mateo, M., Olszewski, E. W., Vogt, S. S., Stubbs, C., & Diercks, A. 1999, *PASP*, 111, 306
- Da Costa, G. S., & Armandroff, T. E. 1990, *AJ*, 100, 162 (DA90)
- Da Costa, G. S., Armandroff, T. E., Caldwell, N., & Seitzer, P. 1996, *AJ*, 112, 2576
- Da Costa, G. S., Armandroff, T. E., Caldwell, N., & Seitzer, P. 2000, *AJ*, 119, 705
- Dekel, A., & Silk, J. 1986, *ApJ*, 303 39
- Dohm-Palmer, R., et al. 1997, *AJ*, 114, 2527
- Dolphin, A. 1997, *NewA*, 2, 397
- Dolphin, A. 2000a, *PASP*, 112, 1383
- Dolphin, A. 2000b, *PASP*, 112, 1397
- Dolphin, A. 2000c, *ApJ*, 531, 804
- Dolphin, A., 2001, *MNRAS*, submitted
- Dolphin, A. et al. 2001a, *ApJ*, 550, 554
- Dolphin, A. et al. 2001b, *MNRAS*, 324, 249
- Ferguson, H. C., & Binggeli, B. 1994, *A&A Rev.*, 6, 67
- Ferguson, H. C., & Sandage, A. 1989, *ApJ*, 346, 53
- Gallagher, G. S., & Wyse, R. F. G. 1994, *PASP*, 106, 1225
- Gallart, C., Martínez-Delgado, D., Gómez-Flechoso, M. A., & Mateo, M. 2001, *AJ*, 121, 2572

- Girardi, L., & Salaris, M. 2001, *MNRAS*, 323, 109
- Girardi, L., Bressan, A., Bertelli, G., & Chiosi, C. 2000, *A&AS*, 141, 371
- Gonzaga, S. et al. 1998, *The Drizzling Cookbook*, ISR WFPC2 98-04 (Baltimore: STScI)
- Grebel, E. K. 1999, *RvMA*, 20, 29
- Held, E. V., Saviane, I., & Momany, Y. 1999, *A&A*, 345, 747
- Hernandez, X., Valls-Gabaud, D., & Gilmore, G. 1999, *MNRAS*, 304, 705
- Hill, R. J., et al. . 1998, *ApJ*, 496, 648
- Hodge, P. 1994, in *Lectures of the Fifth Winter School, Instituto Astrofisco de Canarias* (Cambridge: Cambridge)
- Hodge, P., & Miller, B. W. 1995, *ApJ*, 451, 176
- Holtzman, J. A., et al. 1995, *PASP*, 107, 1065
- Holtzman, J. A., et al. 1997, *AJ*, 113, 656
- Holtzman, J. A., Smith, G. H., & Grillmair, C. 2000, *AJ*, 120, 3060
- Kennicutt, R. C. 1989, *ApJ*, 344, 685
- Kormendy, J. 1985, *ApJ*, 295, 73
- Krist, J. 1995, *ADASS*, 4, 349
- Lee, M. G. 1993, *ApJ*, 408, 409
- Lee, M. G. 1995, *AJ*, 110, 1129
- Lee, M. G., Freedman, W. L, & Madore, B. F. 1993, *ApJ*, 417, 553 (LFM93)
- Lee, Y.-W., Demarque, P., & Zinn, R. 1994, *ApJ*, 423, 248 (LDZ94)
- Leitherer, C., Schaerer, D., Goldader, J. D., González Delgado, R. M., Robert, C., Kune, D. F., de Mello, D. F., Devost, D., & Heckman, T. M. 1999, *ApJS*, 123, 3
- Lin, D. N. C., & Faber S. M. 1983, *ApJ*, 266, 21
- Lo, K. Y., Sargent, W. L. W., & Young, K. 1993, *AJ*, 106, 507
- Martínez-Delgado, D., Gallart, C., & Aparicio, A. 1999, *AJ*, 118, 862
- Mateo, M. 1998, *ARA&A*, 36, 435
- Mathis, J. S. 1990, *ARA&A*, 28, 37
- Miller, B. W., Whitmore, B. C., Schweizer, F., & Fall, S. M. 1997, *AJ*, 114, 2381
- Minniti, D., & Zijlstra, A. A. 1996, *ApJ*, 467, L13
- Mould, J. 1997, *PASP*, 109, 125
- Mould, J., & Kristian, J. 1986, *ApJ*, 305, 591
- Ortolani, S., & Gratton, R. G. 1988, *PASP*, 100, 1405

- Richstone, D. O., & Tremaine, S. 1986, *AJ*, 92, 72
- Salaris, M., & Cassisi, S. 1997, *MNRAS*, 285, 593
- Salzer, J. J., & Norton, S. A. 1999, in *ASP Conf. Ser. 170, Low Surface Brightness Universe*, ed. J. I. Davies, C. Impy, and S. Phillipps (San Francisco: ASP), 253
- Schlegel, D. J., Finkbeiner, D. P., & Davis, M. 1998, *ApJ*, 500, 525
- Schmidt, K.-H., & Boller, T. 1992, *Astr. Nachr.*, 313, 189
- Skillman, E. D., & Bender, R. 1995, *RMxAC*, 3, 25
- Stetson, P. B. 1994, *PASP*, 106, 250
- St-Germain, J., Carignan, C., Côté, S., & Oosterloo, T. 1999, *AJ*, 118, 1235
- Thuan, T. X., & Martin, G. E. 1979, *ApJ*, 232, L11
- Tolstoy, E. & Saha, A. 1996, *ApJ*, 462, 672
- Udalski, A., 2000, *ApJ*, 531, 383
- Vader, J. P. 1986, *ApJ*, 305, 669
- van de Rydt, F., Demers, S., & Kunkel, W. E. 1991, *AJ*, 102, 130
- Whitmore, B., Miller, B. W., Schweizer, F., & Fall, S. M. 1997, *AJ*, 114, 1797
- Wilcots, E. M., & Miller, B. W. 1998, *AJ*, 116, 2363
- Yoshii, Y., & Arimoto, N. 1987, *A&A*, 188, 13
- Young, L. M., & Lo, K. Y. 1996, *ApJ*, 462, 203
- Young, L. M., & Lo, K. Y. 1997, *ApJ*, 490, 710 (YL97)
- Zinn, R., & West, M. J. 1984, *ApJS*, 55, 45

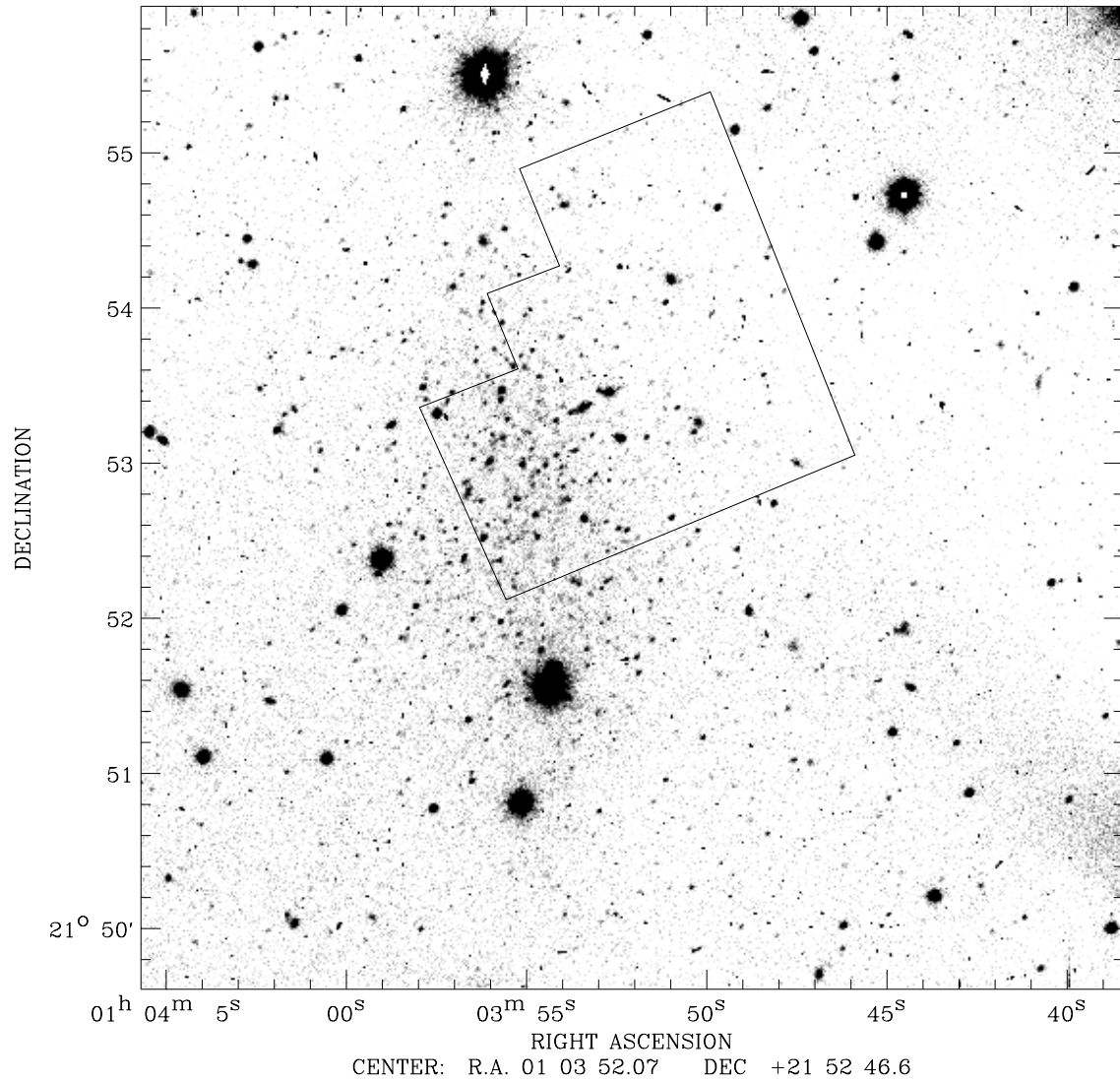


Fig. 1.— An overlay of the WFPC2 footprint on a ground-based *V*-band CCD image of LGS 3 from Lee (1995). The center of the galaxy was placed on the WF2 detector in order to maximize coverage of the galaxy while avoiding the nearby bright stars.

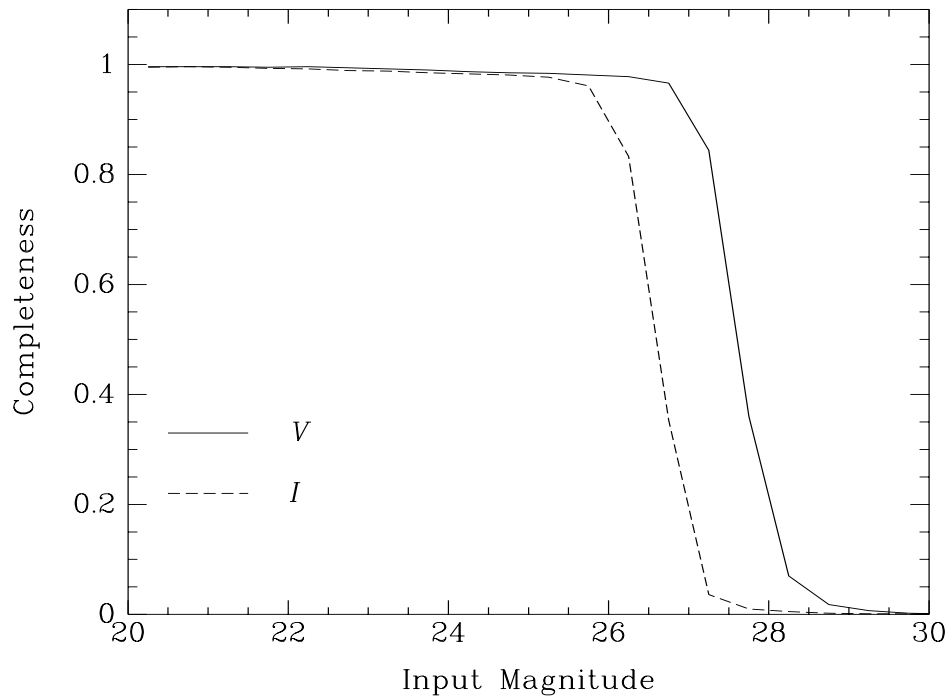


Fig. 2.— Results of artificial-star completeness tests. The 50% completeness limits are  $V \approx 27.6$  and  $I \approx 26.6$ .

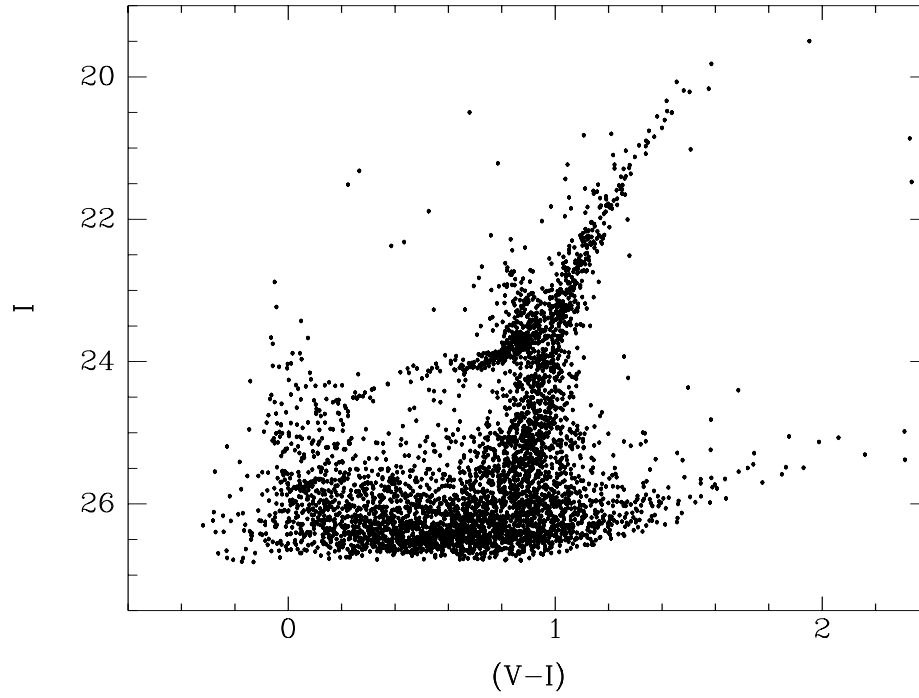


Fig. 3.— Color-magnitude diagram of all stars detected by WFPC2 in LGS 3. The main features are the narrow RGB, a horizontal branch that extends to the blue, a blue plume of young stars, and blue loop and red-clump stars from an intermediate-age population.

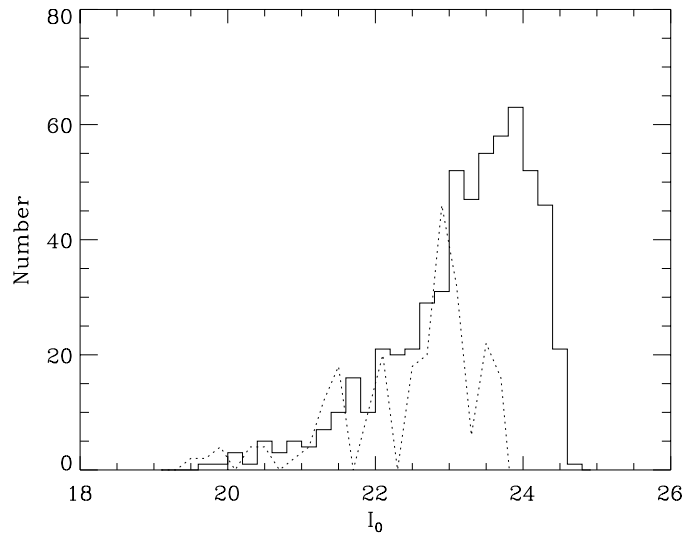


Fig. 4.— The luminosity function of stars in the upper part of the RGB. The small sample size prevents there being a large jump in the LF at the TRGB. As a result, application of a Sobel filter (dotted line), does not produce a strong peak where the TRGB is likely to be. It is most likely that the TRGB has  $I \approx 20$  or  $I \approx 20.5$ .

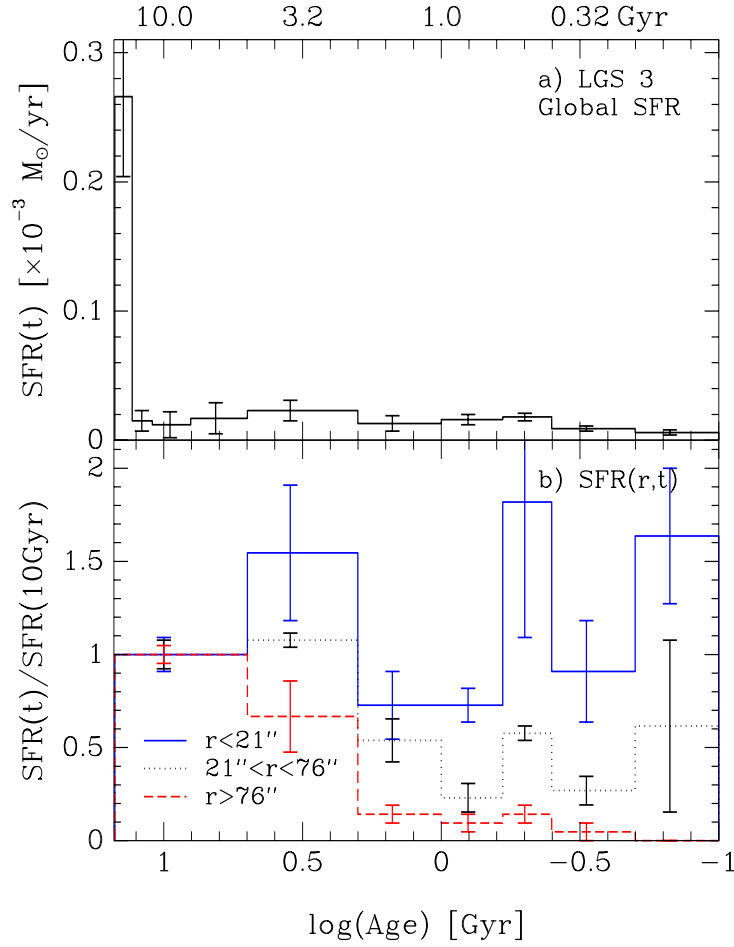


Fig. 5.— The star formation rate as function of time as derived from the least-squares fits to the CMD. a) The global solution (Table 3). b) Solutions for three radial bins, normalized to the SFR in the 5–15 Gyr bin (Table 4). The different binning is produced by averaging the previous bins rather than running new solutions with different bin sizes.

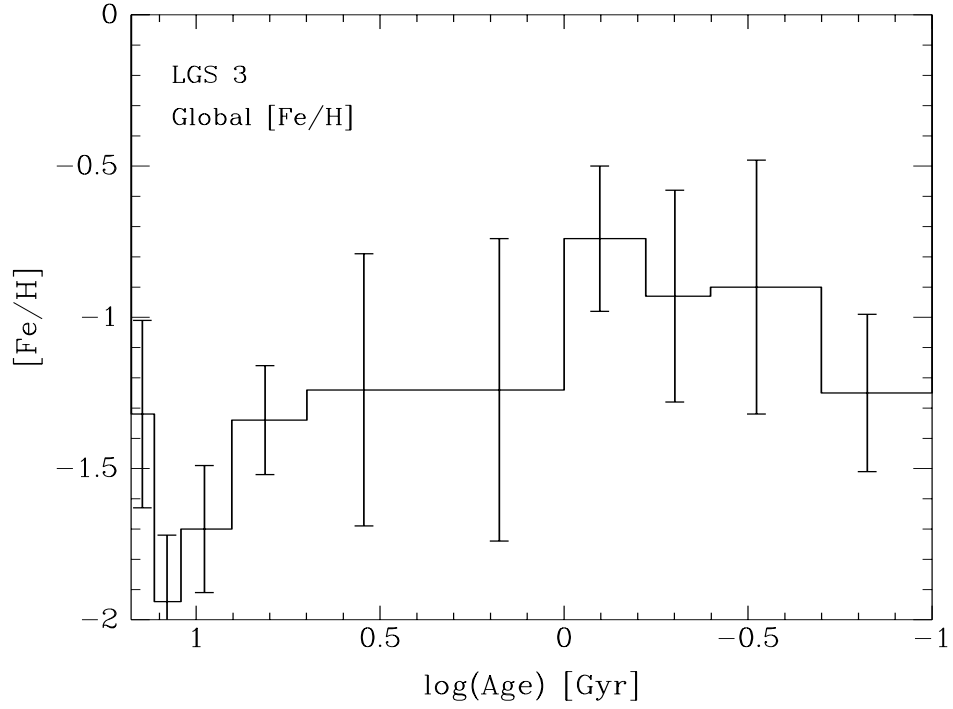


Fig. 6.— The global metallicity as a function of time from the least-squares fits to the CMD.

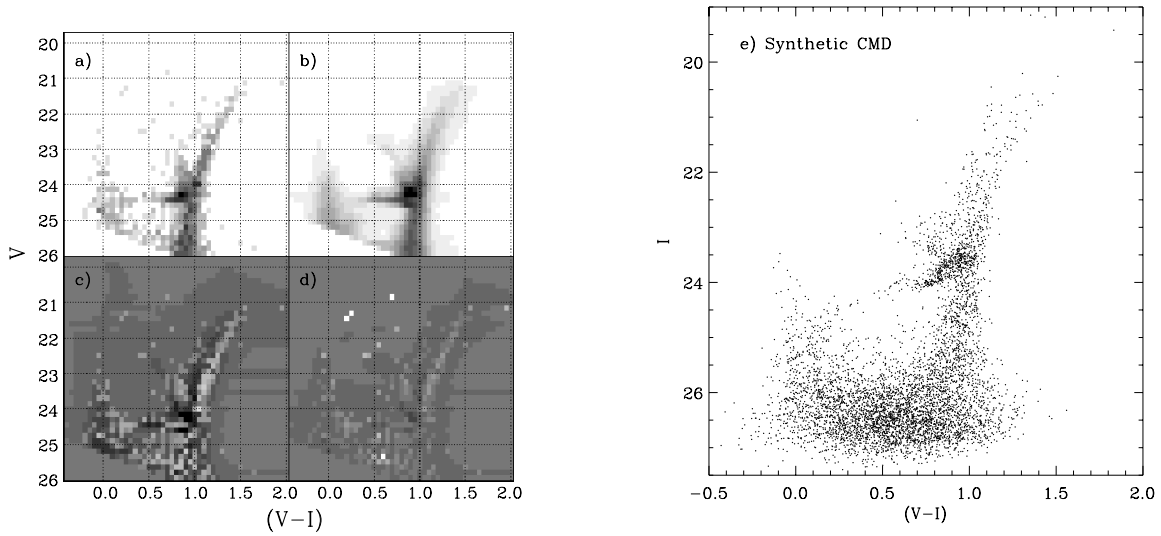


Fig. 7.— a-d) High resolution (e-h) Hess diagrams showing the comparison between the observed and modeled CMDs. a) observations; b) best-fit synthetic; c) residuals (light = more observed; dark = more synthetic); d) residuals in terms of sigma, the darkest shades correspond to a  $3\sigma$  difference. e) An example synthetic CMD from the best model.

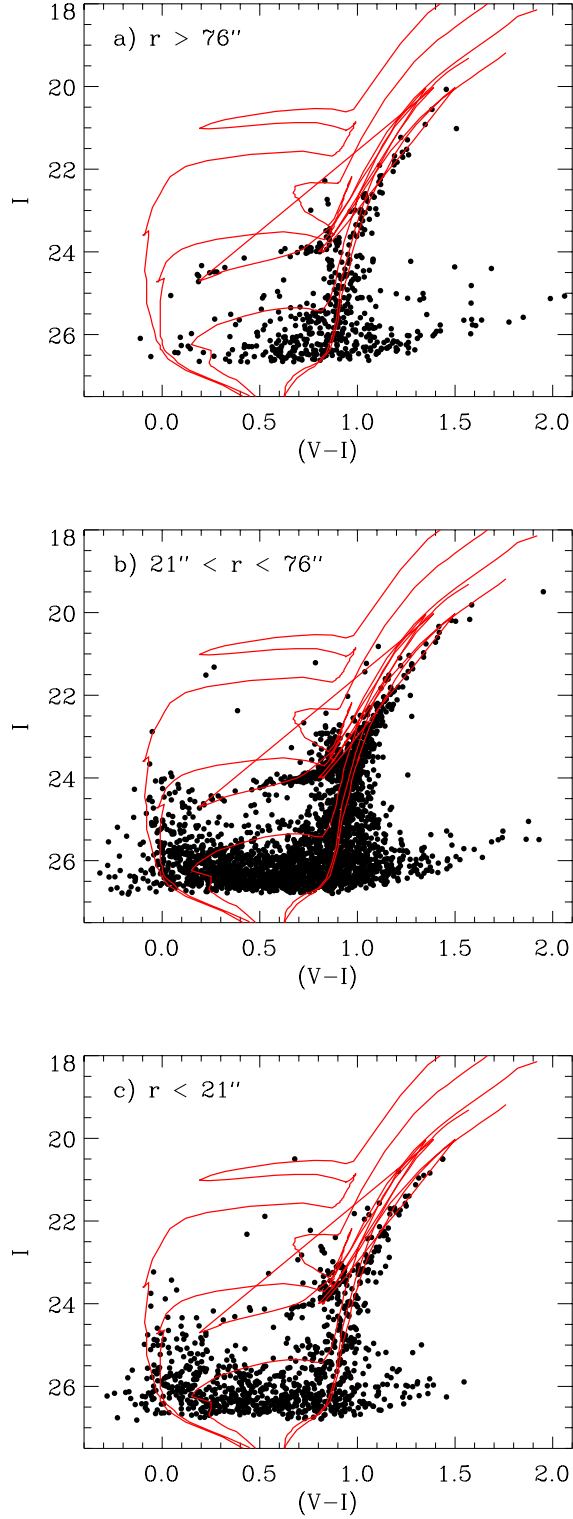


Fig. 8.— CMDs of stars in different radial bins with isochrones from Girardi et al. (2000) over-plotted.  $(Z, \log(t))$  for the models are  $(0.001, 8.3)$ ,  $(0.001, 8.8)$ ,  $(0.001, 9.4)$ ,  $(0.001, 10.1)$ , and  $(0.0004, 10.2)$ . The models have been shifted to match the data using  $(m - M)_0 = 23.96$  and  $E(B - V) = 0.04$ . a)  $r > 76''$ ; b)  $21'' < r < 76''$ ; and c)  $r < 21''$ .

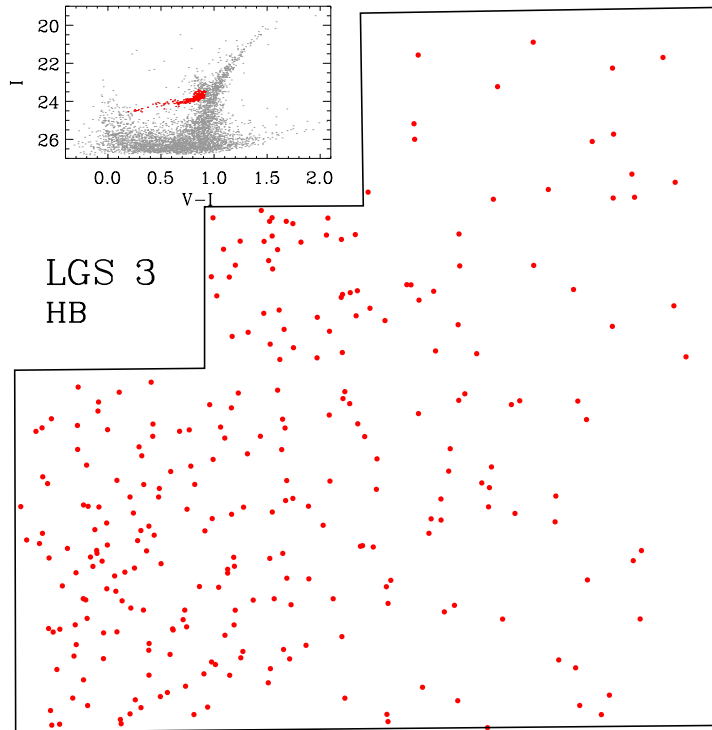


Fig. 9.— CMD and spatial distribution of the horizontal branch stars. These stars are the most uniformly distributed type in LGS 3.

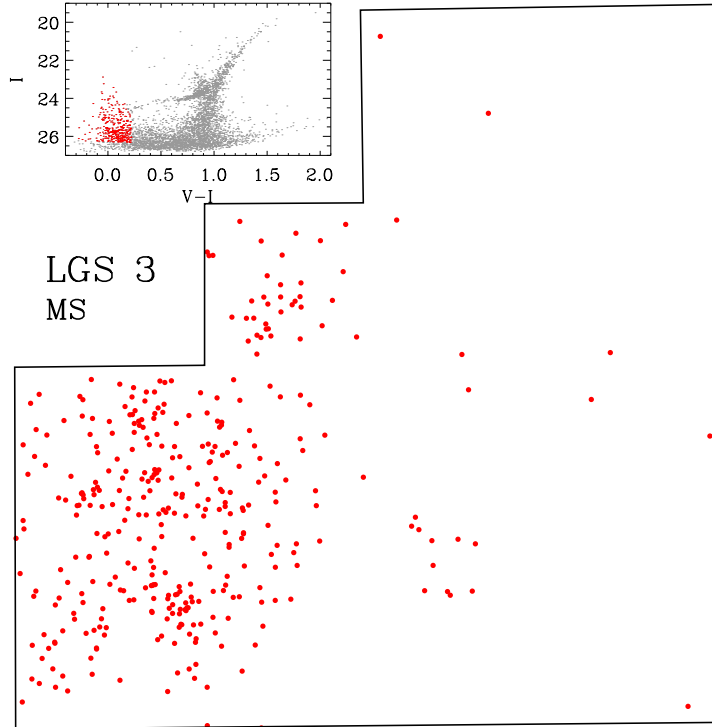


Fig. 10.— CMD and spatial distribution of the main sequence stars showing clear groupings near the center of the galaxy.

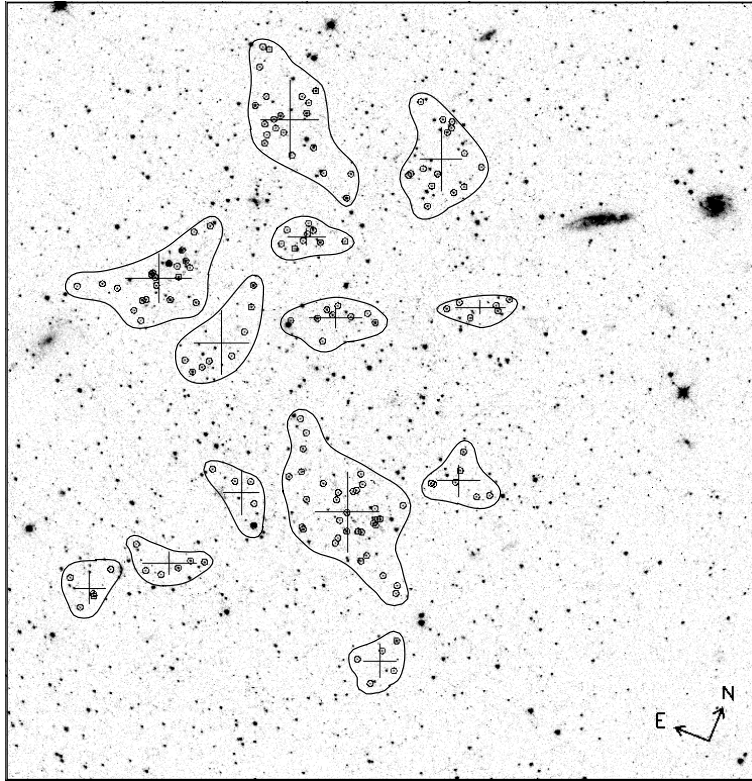


Fig. 11.— Clusters of blue stars found in WF2 using the PLC method (Battinelli 1991). Circled stars are the members of the clusters and the boundaries are drawn by eye to help distinguish them. Crosses give the centroids of the clusters and the sigmas in x and y. The PLC scale length is  $d_s = 4.1$  pc, but the largest linear dimension of a cluster can be up to 27 pc (Table 5).

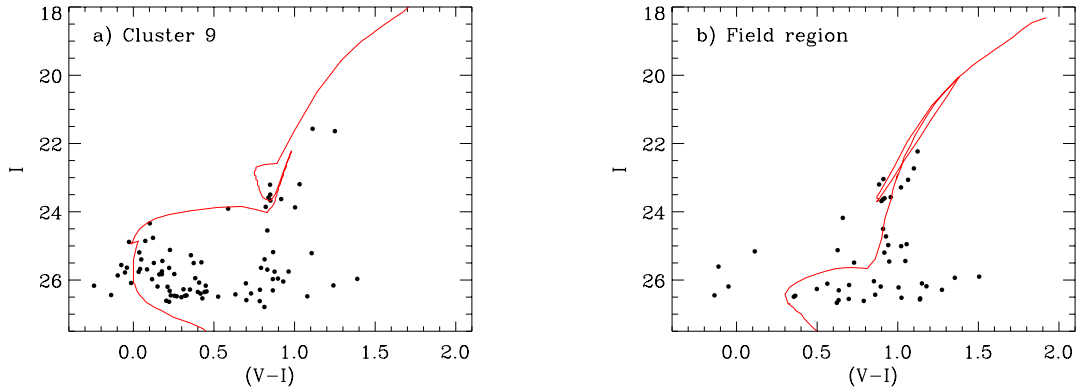


Fig. 12.— a) CMD of stars in Cluster 9, the largest of the young stellar groupings (Table 5). Overplotted is an isochrone from Girardi et al. (2000) with  $Z = 0.001$ ,  $\log(t) = 8.9$ ,  $(m - M)_0 = 23.96$ , and  $E(B - V) = 0.04$ . The match suggests that the age of the cluster is about 800 Myr. b) A CMD of region of WF2 of comparable size to that used in (a), but not containing any clusters. The isochrone is for  $Z = 0.001$ ,  $t = 3.5$  Gyr and the good match suggests that most of the stars in this region are older than a few Gyr.

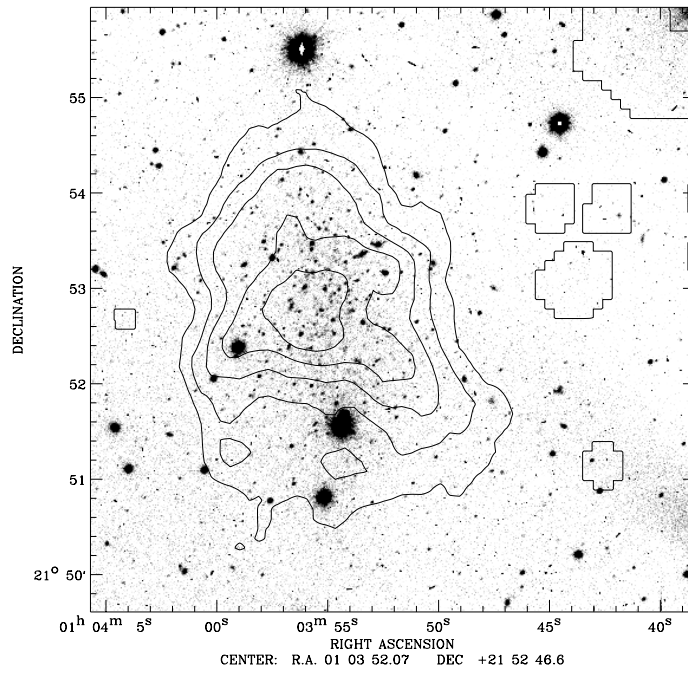


Fig. 13.— Contours of H I column density from Young & Lo (1997) superposed on the ground-based  $V$  image from Lee (1995). Unlike other dI galaxies with gas, the H I has a smooth distribution that follows the stellar distribution. Contour levels are  $2.5, 5.0, 7.5, 10.0,$  and  $12.5 \times 10^{19} \text{ cm}^{-2}$ .

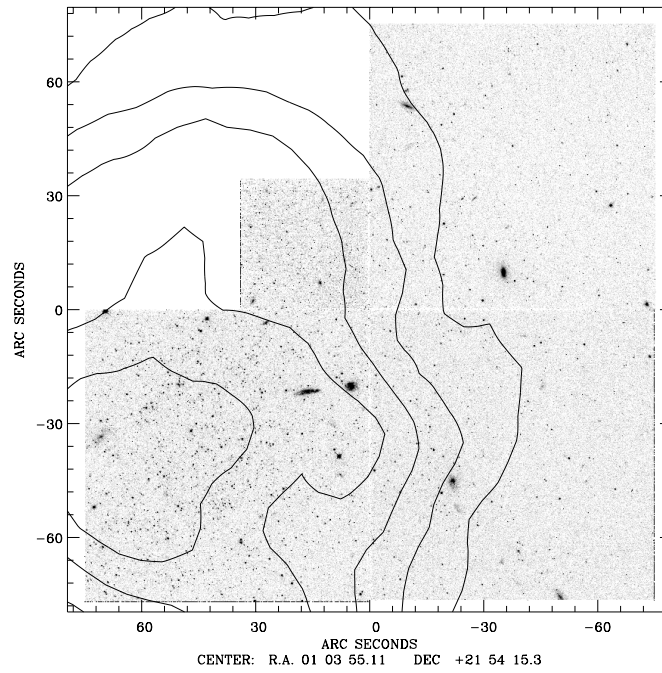


Fig. 14.— Contours of H I column density from Young & Lo (1997) superposed on the WFPC2 image. The most recent star formation and the central clusters are near the region of highest H I column density. Contour levels are  $2.5, 5.0, 7.5, 10.0,$  and  $12.5 \times 10^{19} \text{ cm}^{-2}$ .

Table 1. Photometry Comparisons

Detector	$\delta V$	$\delta(V - I)$	$\delta I$	Comments
HSTphot –ALLFRAME				
PC	$-0.23 \pm 0.04$	$-0.02 \pm 0.04$	$-0.22$	$20 < V < 25, 20 < I < 24$
WF	$-0.09 \pm 0.02$	$0.00 \pm 0.01$	$-0.09 \pm 0.02$	
HSTphot –Aperture				
PC	$-0.14 \pm 0.03$	$+0.06 \pm 0.03$	$-0.20 \pm 0.03$	$V < 25$
WF	$+0.00 \pm 0.06$	$+0.03 \pm 0.05$	$-0.03 \pm 0.06$	
HSTphot –Lee(1995)				
WF2	$+0.02 \pm 0.11$	$+0.02$	$+0.00 \pm 0.16$	$20 < V < 22.8, 19 < I < 22$
HSTphot –Aparicio et al. (1997)				
WF	$-0.07$	$-0.05$	$-0.02$	
HSTphot –Mould (1997)				
WF	$-0.24$	$0.02$	$-0.26$	

Table 2. Summary of Distance Estimates

Method	$E(B - V)$	$(m - M)_0$	Distance (kpc)
TRGB	0.04	$24.08 \pm 0.30$	$655 \pm 90$
HB	0.04	$23.98 \pm 0.10$	$625 \pm 30$
RC	0.04	$23.96 \pm 0.12$	$620 \pm 30$
SFH	0.04	$23.93 \pm 0.07$	$610 \pm 20$

Table 3. Global SFH

Age Range (Gyr)	SFR ( $\times 10^{-5} M_{\odot} \text{ yr}^{-1}$ )	mean [Fe/H]	$\sigma$ ([Fe/H])
0.1 – 0.2	$0.6 \pm 0.2$	$-1.25 \pm 0.50$	$0.26 \pm 0.31$
0.2 – 0.4	$0.9 \pm 0.2$	$-0.90 \pm 0.08$	$0.42 \pm 0.03$
0.4 – 0.6	$1.8 \pm 0.3$	$-0.93 \pm 0.07$	$0.35 \pm 0.08$
0.6 – 1.0	$1.6 \pm 0.4$	$-0.74 \pm 0.10$	$0.24 \pm 0.09$
1.0 – 2.0	$1.3 \pm 0.6$	$-1.24 \pm 0.26$	$0.50 \pm 0.13$
2.0 – 5.0	$2.3 \pm 0.8$	$-1.24 \pm 0.15$	$0.45 \pm 0.09$
5.0 – 8.0	$1.7 \pm 1.2$	$-1.34 \pm 0.22$	$0.18 \pm 0.15$
8.0 – 11.0	$1.2 \pm 1.0$	$-1.70 \pm 0.25$	$0.21 \pm 0.16$
11.0 – 13.0	$1.5 \pm 0.8$	$-1.94 \pm 0.40$	$0.22 \pm 0.15$
13.0 – 15.0	$26.6 \pm 6.2$	$-1.32 \pm 0.10$	$0.31 \pm 0.07$

Note. —  $A_V = 0.11$ ,  $(m - M)_0 = 23.94$ , IMF slope = 1.35

Table 4. Radial SFH

Age Range (Gyr)	SFR/SFR(10Gyr)		
	$r < 21''$	$21'' < r < 76''$	$r > 76''$
0.1 – 0.2	$1.64 \pm 0.36$	$0.62 \pm 0.46$	$0.00 \pm 0.00$
0.2 – 0.4	$0.91 \pm 0.27$	$0.27 \pm 0.08$	$0.05 \pm 0.05$
0.4 – 0.6	$1.82 \pm 0.73$	$0.58 \pm 0.04$	$0.14 \pm 0.05$
0.6 – 1.0	$0.73 \pm 0.09$	$0.23 \pm 0.08$	$0.10 \pm 0.05$
1.0 – 2.0	$0.73 \pm 0.18$	$0.54 \pm 0.12$	$0.14 \pm 0.05$
2.0 – 5.0	$1.55 \pm 0.36$	$1.08 \pm 0.04$	$0.67 \pm 0.19$
5.0 – 15.0	$1.00 \pm 0.09$	$1.00 \pm 0.08$	$1.00 \pm 0.05$

Table 5. Clusters with  $V - I < 0.3$ ,  $I < 26$ ,  $d_s = 4.1$  pc, and  $N_{star} > 5$

Id	$N_{star}$	RA (J2000)	Dec (J2000)	$\sigma(x)$ [pc]	$\sigma(y)$ [pc]	$D_{max}$ [pc]
1	21	01:03:56.185	21:52:58.06	4.4	3.2	19.8
2	5	01:03:55.068	21:52:41.66	2.4	3.0	9.4
3	8	01:03:55.602	21:52:54.55	3.7	4.3	14.3
4	9	01:03:54.916	21:53:01.07	3.5	1.4	11.5
5	21	01:03:55.752	21:53:17.43	3.9	5.3	23.4
6	5	01:03:53.704	21:52:31.45	2.2	2.3	6.8
7	9	01:03:55.325	21:53:07.36	2.6	1.1	8.6
8	6	01:03:55.347	21:52:32.48	3.6	1.4	9.6
9	33	01:03:54.320	21:52:43.80	4.3	5.4	26.9
10	15	01:03:54.653	21:53:19.51	2.8	4.2	14.2
11	6	01:03:54.000	21:53:07.43	3.4	0.9	8.6
12	7	01:03:53.674	21:52:50.85	2.9	2.1	8.1
13	5	01:03:55.801	21:52:27.17	2.1	2.1	6.6

Table 6. General Properties of LGS 3.

Parameter	Value	Units	Source
Observed			
Distance modulus	$23.96 \pm 0.07$	mag	1
Distance	$620 \pm 20$	kpc	1
Foreground reddening	$0.04 \pm 0.01$	mag	1,2
$V$ integrated ( $r < 106''$ )	$14.26 \pm 0.04$	mag	3
Core radius	$0.82 \pm 0.05$	arcmin	3
Ellipticity	$0.2 \pm 0.1$		3
$V$ central surface brightness	$24.8 \pm 0.1$	mag arcsec <sup>-2</sup>	3
Central velocity dispersion	$2.6 - 30.5$	km s <sup>-1</sup>	4
“Most likely” velocity dispersion	$7.9^{+5.3}_{-2.9}$	km s <sup>-1</sup>	4
Optical systemic velocity	$-282 \pm 4$	km s <sup>-1</sup>	4
HI systemic velocity	$-286.5 \pm 0.3$	km s <sup>-1</sup>	5
Integrated HI flux	$2.7 \pm 0.1$	Jy km s <sup>-1</sup>	5
Derived			
Absolute magnitude ( $M_V$ )	$-9.82 \pm 0.09$	mag	
Core radius	$148 \pm 9$	pc	
Central surface brightness ( $S_{0,V}$ )	$4.4 \pm 0.8$	$L_{\odot V}$ pc <sup>-2</sup>	
Central mass density ( $\rho_0$ )	$0.05 - 6.9$	$M_{\odot}$ pc <sup>-3</sup>	
Total mass	$2.8 \times 10^6 - 3.9 \times 10^8$	$M_{\odot}$	
“Most likely” mass	$(2.6^{+4.7}_{-1.6}) \times 10^7$	$M_{\odot}$	
Central luminosity density	$0.014 \pm 0.003$	$L_{\odot V}$ pc <sup>-3</sup>	
Central $M/L$	$3.6 - 490$	$M_{\odot}/L_{\odot V}$	
Total luminosity	$(7.2 \pm 0.6) \times 10^5$	$L_{\odot V}$	
Integrated $M/L$	$3.9 - 535$	$M_{\odot}/L_{\odot V}$	
“Most likely” $M/L$	$36^{+64}_{-22}$	$M_{\odot}/L_{\odot V}$	
Asymptotic $M/L$	$140^{+252}_{-84}$	$M_{\odot}/L_{\odot V}$	
Total gas mass (incl. He)	$(3.4 \pm 0.2) \times 10^5$	$M_{\odot}$	
Gas mass fraction	$9 \times 10^{-4} - 0.1$		

References. — (1) This work; (2) Schlegel et al. 1998; (3) Lee 1995; (4) Cook et al. 1999; (5) Young & Lo 1997